

Ab initio Ultrafast Spin Dynamics in Solids

Junqing Xu^{‡,1}, Adela Habib^{‡,2}, Ravishankar Sundararaman^{†,3}, and Yuan Ping^{*1}

¹*Department of Chemistry and Biochemistry, University of California, Santa Cruz, CA 95064, USA*

²*Department of Physics, Applied Physics and Astronomy,
Rensselaer Polytechnic Institute, 110 8th Street, Troy, New York 12180, USA*

³*Department of Materials Science and Engineering,
Rensselaer Polytechnic Institute, 110 8th Street, Troy, New York 12180, USA*

(Dated: June 29, 2022)

Spin relaxation and decoherence is at the heart of spintronics and spin based quantum information science. Currently, no theoretical approaches can accurately predict spin relaxation of solids including necessary scattering pathways for required ns to ms simulation time. We present a first-principles real-time density-matrix approach based on Lindblad dynamics to simulate ultrafast spin dynamics including various scattering processes for general solid-state systems. Through the complete theoretical descriptions of pump, probe and scattering processes including electron-phonon, electron-impurity and electron-electron scatterings, our method can directly simulate the ultrafast pump-probe measurements for coupled spin and electron dynamics at any temperatures and doping levels. We apply this method to a prototypical system GaAs and obtain excellent agreement with experiments. We found that the relative contributions of different scattering mechanisms and phonon modes vary considerably between spin and carrier relaxation processes. Importantly, in sharp contrast to previous work based on model Hamiltonians, we point out that at low temperatures the electron-electron scattering becomes very important for spin relaxation. Most importantly, we examine the applicable conditions of the commonly-used phenomenological D'yakonov-Perel' relation, which may break down for individual scattering processes. Our work provides a predictive computational platform for spin relaxation in solids, which has unprecedented potentials for designing new materials ideal for spintronics and quantum information technology.

I. INTRODUCTION

Spin is a fundamental quantum mechanical property of electrons and other particles. The spin states can be used as the basis of quantum bits in quantum information science (QIS)¹, in addition to being used in spintronics analogous to electrical charge in conventional electronics². The key property for spintronics and quantum information science is the lifetime of spin states. Determining the underlying mechanisms and controlling spin relaxation is vital to reach long spin lifetimes at room temperature: stable manipulation of spin states in practical applications require lifetimes on the order of over hundreds of nanoseconds or microseconds. Experimentally spin relaxation can be studied through ultrafast magneto-optical pump-probe^{3,4} and spin transport measurements⁵, allowing the direct observations of dynamical processes and quantitative determination of spin relaxation time, τ_s .

Currently no materials with ideal spin properties are known for QIS and spintronics applications, although significant experimental progress has been made and several systems were proposed in the past decades^{1,2,6}. Theoretical predictions have been more focused on electronic excitations^{7,8} and electron-hole recombinations^{9–11} of potential spin defects for QIS applications. Reliable prediction of spin lifetime will allow rational design of materi-

als to accelerate the identification of ideal materials for quantum technologies, while forgoing the need of experimental search over a large number of materials.

Until recently, only simplified and system-specific models that require prior input parameters have been used to calculate spin lifetime of solid-state materials^{2,12–15}. These methods laid important theoretical foundation for spin dynamics, such as the spin-Bloch kinetic equations developed from Non-equilibrium Green's Function theory (NEGFT)¹⁶. However, because of the simplified electronic structure and electron-phonon coupling matrices, while the obtained results provide qualitatively important insights, they hardly yield quantitatively accurate values to compare with experiments. Furthermore, these models are unable to provide predictive values for new materials where prior inputs are not available. Prior to our work, the existing first-principles methodology has been based on spin-flip matrix elements in a specialized Fermi's Golden rule^{17–19}, which is only applicable to systems with Kramers' degeneracy or spatial inversion symmetry, not applicable to most materials promising for quantum computing and spintronics applications^{2,6}. Other techniques like real-time Time-Dependent Density Functional Theory (TDDFT)^{20,21} are challenging for crystalline systems due to high computational cost for describing phonon relaxations that require large supercells, in addition to the long simulation time over nanoseconds often required for spin dynamics. While spin dynamics based on TDDFT has been recently performed for ultrafast demagnetization of magnetic systems^{22–24}, the intrinsic time scale and supercell limitations mentioned above remain.

[‡]JX and AH contributed equally to this work.

[†]sundar@rpi.edu

^{*}yuanping@ucsc.edu

We recently developed a first-principles framework²⁵ based on density matrix (DM) Lindblad dynamics^{26,27} that can be generalized to any phase-sensitive quantum mechanical observables that couple with environmental degrees of freedom. From this framework, we derived a generalized rate equation that provides accurate spin relaxation time due to spin-orbit and electron-phonon couplings for a broad range of materials, with arbitrary symmetry, entirely from first-principles. In this work, we develop this framework to the next critical stage, with complete theoretical descriptions of scattering processes including electron-phonon (e-ph), electron-impurity (e-i) and electron-electron (e-e) in real-time simulations. Compared to the generalized rate equation, DM dynamics with explicit real-time evolutions allows coupled carrier and spin relaxation away from quasi-equilibrium with all decoherence pathways simultaneously. This will facilitate direct prediction of experimental signatures in ultrafast magneto-optical spectroscopy to unambiguously interpret experimental probes of spin and electron dynamics.

As a showcase, in this paper we will apply our DM dynamics methodology to investigate ultrafast spin dynamics of GaAs. It has broad interest in spintronics² due to its long spin lifetime, especially in the n-doped material at relatively low temperature²⁸. Despite various experimental^{28–32} and theoretical^{2,33–37} studies previously, the dominant spin relaxation mechanism of GaAs under various temperatures and doping levels remains unclear. For example, Refs. 34 and 36 claimed e-i and e-ph scatterings dominate spin relaxation at low and room temperatures, respectively; however, Ref. 37 concludes that e-e may be more important at room temperature. Moreover, electron-phonon scattering matrices which can be accurately obtained by first-principles electron-phonon matrix elements with self-consistent spin-orbit coupling, are very difficult to be accurately described in parameterized models. Most importantly, the applicability of empirical D'yakonov-Perel' (DP) relation, which is widely used for describing inversion asymmetric systems including GaAs, has not been examined carefully. Here, we provide complete and unbiased insights on the underlying mechanism of spin relaxation and applicability of the DP relation for GaAs from first-principles DM dynamics.

In the following, we first introduce our theoretical formalism of real-time density matrix approach with various scattering processes and pump-probe spectroscopy. In particular, we focus on spin-orbit mediated spin relaxation and decoherence processes with various scatterings, which are rather common in semiconductors and metals^{2,16}. We use this method to simulate pump-probe Kerr rotation and real-time spin dynamics, by using GaAs as a prototypical example and comparing with experiments. Next, we study the temperature and doping-level dependence of spin lifetime, where the doping concentration is adjusted by the Fermi level position. At the end, we discuss the roles of different scattering mechanisms and phonon modes at various temperature and

doping levels in carrier and spin relaxations, respectively. Our work provides predictive theory and computational platform for quantum dynamics, offers new and unbiased insights for spin relaxation and decoherence in general solid-state systems.

II. THEORY

A. Real-time density-matrix dynamics and spin relaxation time

To provide a general formulation of quantum dynamics in solid-state materials, we start from the Liouville-von Neumann equation in the interaction picture,

$$\frac{d\rho(t)}{dt} = -i[H'(t), \rho(t)], \quad (1)$$

$$H'(t) = H(t) - H_0(t), \quad (2)$$

where H , H_0 and H' are total, unperturbed and perturbed Hamiltonian, respectively. In this work, the total Hamiltonian is

$$H = H_0 + H_{\text{pump}} + H_{\text{e-i}} + H_{\text{e-ph}} + H_{\text{e-e}}, \quad (3)$$

$$H_0 = H_e + H_z + H_{\text{ph}}, \quad (4)$$

where H_e is electronic Hamiltonian under zero field. Above, H_z is the Zeeman Hamiltonian corresponding to an external magnetic field \mathbf{B} , $H_z = g_s \mu_B \mathbf{B} \cdot \mathbf{s}$, where $\mathbf{s} = (s_x, s_y, s_z)$ and s_i is spin matrix in Bloch basis under zero field. H_{pump} is the Hamiltonian of the pump pulse and will be described below. H_{ph} is the phonon Hamiltonian, while $H_{\text{e-i}}$, $H_{\text{e-ph}}$ and $H_{\text{e-e}}$ describe the electron-impurity, electron-phonon and electron-electron interactions respectively. The detailed forms of the interaction Hamiltonians are given in Appendix A.

In practice, the many-body density matrix master equation in Eq. 1 is reduced to a single-particle one and the environmental degrees of freedom are traced out³⁸. The total rate of change of the density matrix is separated into terms related to different parts of Hamiltonian,

$$\frac{d\rho}{dt} = \frac{d\rho}{dt}|_{\text{coh}} + \frac{d\rho}{dt}|_{\text{scatt}}, \quad (5)$$

where ρ is the density matrix of electrons. Above, $\frac{d\rho}{dt}|_{\text{coh}}$ describes the coherent dynamics of electrons under potentials or fields, e.g. the applied pump pulse, while $\frac{d\rho}{dt}|_{\text{scatt}}$ captures the scattering between electrons and other particles.

To define spin lifetime, we follow the time evolution of the observable

$$S_i = \text{Tr}(s_i \rho), \quad (6)$$

where s_i is the spin operator ($i = x, y, z$). This time evolution must start at an initial state (at $t = t_0$) with a net spin i.e. $\delta\rho(t_0) = \rho(t_0) - \rho^{\text{eq}} \neq 0$ such that $\delta S_i(t_0) =$

$S_i(t_0) - S_i^{\text{eq}} \neq 0$, where “eq” corresponds to the final equilibrium state. We evolve the density matrix through Eq. 5 for a long enough simulation time, typically from tens of ps to hundreds of ns, until the evolution of $S_i(t)$ can be reliably fit by

$$S_i(t) - S_i^{\text{eq}} = [S_i(t_0) - S_i^{\text{eq}}] \exp\left[-\frac{t-t_0}{\tau_{s,i}}\right] \times \cos[\omega_B(t-t_0) + \phi]. \quad (7)$$

to extract the relaxation time, $\tau_{s,i}$. Above, ω_B is oscillation frequency due to energy splitting in general, which under an applied magnetic field \mathbf{B} would include a contribution $\approx 0.5g_s\mu_B(\mathbf{B} \times \hat{\mathbf{S}}_i)$.

We implement two general ways to initialize $\delta\rho(t_0)$. First, for simulating pump-probe experiments, we choose $\delta\rho(t_0)$ corresponding to interaction with a pump pulse. Second, we use the technique proposed previously in Ref. 25 by applying a test magnetic field at $t = -\infty$, allowing the system to equilibrate with a net spin and then turning it off suddenly at t_0 .

B. Scattering terms

The scattering part of the master equation can be separated into contributions from several scattering channels,

$$\frac{d\rho}{dt}|_{\text{scatt}} = \sum_c \frac{d\rho}{dt}|_c, \quad (8)$$

where c labels a scattering channel. Under Born-Markov approximation²⁶, in general we have^{27,39}

$$\frac{d\rho_{12}}{dt}|_c = \frac{1}{2} \sum_{345} \begin{bmatrix} (I-\rho)_{13} P_{32,45}^c \rho_{45} \\ -(I-\rho)_{45} P_{45,13}^{c,*} \rho_{32} \end{bmatrix} + H.C., \quad (9)$$

where P^c is the generalized scattering-rate matrix and H.C. is Hermitian conjugate. The subindex, e.g., “1”, is the combined index of k-point and band. The weights of k points must be considered when doing sum over k points. Note that P^c in the interaction picture is related to its value $P^{S,c}$ in the Schrodinger picture as

$$P_{1234}^c(t) = P_{1234}^{S,c} \exp[it(\epsilon_1 - \epsilon_2 - \epsilon_3 + \epsilon_4)], \quad (10)$$

where ϵ_i are single-particle eigenvalues of H_0 . Below, we consider three separate scattering mechanisms - electron-impurity (e-i), electron-phonon (e-ph) and electron-electron (e-e), and describe the matrix elements for each.

For electron-phonon scattering, the scattering matrix is given by²⁷

$$P_{1234}^{S,e-ph} = \sum_{q\lambda\pm} A_{13}^{q\lambda\pm} A_{24}^{q\lambda\pm,*}, \quad (11)$$

$$A_{13}^{q\lambda\pm} = \sqrt{\frac{2\pi}{\hbar}} g_{12}^{q\lambda\pm} \delta^{G,1/2}(\epsilon_1 - \epsilon_2 \pm \omega_{q\lambda}) \sqrt{n_{q\lambda}^{\pm}}, \quad (12)$$

where q and λ are phonon wavevector and mode, $g^{q\lambda\pm}$ is the electron-phonon matrix element, resulting from the absorption (−) or emission (+) of a phonon, computed with self-consistent spin-orbit coupling from first-principles,⁴⁰ $n_{q\lambda}^{\pm} = n_{q\lambda} + 0.5 \pm 0.5$ in terms of phonon Bose factors $n_{q\lambda}$, and δ^G represents an energy conserving δ -function broadened to a Gaussian of width σ .

Next, for electron-impurity scattering, the scattering matrix is given by

$$P_{1234}^{S,e-i} = A_{13}^i A_{24}^{i,*}, \quad (13)$$

$$A_{13}^i = \sqrt{\frac{2\pi}{\hbar}} g_{13}^i \delta^{G,1/2}(\epsilon_1 - \epsilon_3) \sqrt{n_i V_{\text{cell}}}, \quad (14)$$

$$g_{13}^i = \langle 1 | V^i | 3 \rangle, \quad (15)$$

where n_i and V_{cell} are impurity density and unit cell volume, respectively, and V^i is the impurity potential. In this work, we will deal with only ionized impurities, and V^i is proportional to screened Coulomb potential.⁴¹ (See Appendix A for further details).

Finally, for electron-electron scattering, the scattering matrix is given by²⁷

$$P_{12,34}^{S,e-e} = 2 \sum_{56,78} (I-\rho)_{65} \mathcal{A}_{15,37} \mathcal{A}_{26,48}^* \rho_{78}, \quad (16)$$

$$\mathcal{A}_{1234} = \frac{1}{2} (A_{1234} - A_{1243}), \quad (17)$$

$$A_{1234} = \frac{1}{2} \sqrt{\frac{2\pi}{\hbar}} \left(g_{1234}^{e-e} \delta_{1234}^{G,1/2} + g_{2143}^{e-e} \delta_{2143}^{G,1/2} \right), \quad (18)$$

$$g_{1234}^{e-e} = \langle 1(r) | \langle 2(r') | V(r-r') | 3(r) \rangle | 4(r') \rangle, \quad (19)$$

where $V(r-r')$ is the screened Coulomb potential and $\delta_{1234}^G = \delta^G(\epsilon_1 + \epsilon_2 - \epsilon_3 - \epsilon_4)$ is a Gaussian-broadened energy conservation function. The screening is described by Random-Phase-Approximation (RPA)⁴² dielectric function (details in Appendix A). Although the above equations describe all possible scattering processes between electrons and holes, we only consider those between conduction electrons here, which is appropriate for n-type Group III-V semiconductors^{34,36}. The electron-hole scattering can be important for intrinsic and p-type material.^{34,36} We note that unlike the previous channels, $P^{S,e-e}$ is a function of ρ and needs to be updated during time evolution of ρ . This is a clear consequence of the two-particle nature of e-e scattering. $P^{S,e-e}$ can be written as the difference between a direct term and an exchange term,

$$P^{S,e-e} = P^{S,e-e,d} - P^{S,e-e,x}, \quad (20)$$

$$P^{S,e-e,d} = \sum_{56,78} (I-\rho)_{65} A_{15,37} A_{26,48}^* \rho_{78}, \quad (21)$$

$$P^{S,e-e,x} = \sum_{56,78} (I-\rho)_{65} A_{15,37} A_{26,84}^* \rho_{78}. \quad (22)$$

According to Ref. 38, the direct term is expected to dominate the dynamic scattering processes between conduction or valence electrons, allowing us to neglect the exchange term here.

C. Pump-probe simulation

The interaction with a pump pulse of frequency ω_{pump} in the interaction picture is given by

$$H_{\text{pump},k,mn}(\omega_{\text{pump}}, t) = \frac{e}{m_e} \mathbf{A}_0(t) \cdot \mathbf{p}_{k,mn} e^{it(\epsilon_m - \epsilon_n - \omega_{\text{pump}})} + H.C., \quad (23)$$

where \mathbf{p} is the momentum operator matrix and $\mathbf{A}_0(t)$ is the vector potential. For a Gaussian pulse centered at time t_{center} with width τ_{pump} ,

$$\mathbf{A}_0(t) = \mathbf{A}_0 \frac{1}{\sqrt{\pi\tau_{\text{pump}}}} \exp\left[-(t - t_{\text{center}})^2 / (2\tau_{\text{pump}}^2)\right]. \quad (24)$$

Note that the corresponding pump power is $I = \omega_{\text{pump}}^2 |A_0|^2 / (8\pi\alpha)$, where α is fine structure constant. As a part of the coherent portion of the time evolution, the dynamics due to this term are captured directly in the Liouville form,⁴³

$$\frac{d\rho}{dt}|_{\text{pump}} = -i[H_{\text{pump}}, \rho]. \quad (25)$$

The probe pulse interacts with the material similarly to the pump pulse, and could be described in exactly the same way in principle. However, this would require repeating the simulation for several values of the pump-probe delay. Instead, since the probe is typically chosen to be of sufficiently low intensity, we use second-order time-dependent perturbation theory to capture its interaction with the system,

$$\Delta\rho^{\text{probe}} = \frac{1}{2} \sum_{345} \left\{ \begin{array}{l} [I - \rho(t)]_{13} P_{32,45}^{\text{probe}} \rho(t)_{45} \\ - [I - \rho(t)]_{45} P_{45,13}^{\text{probe},*} \rho(t)_{32} \end{array} \right\} + H.C., \quad (26)$$

where P^{probe} is the generalized scattering-rate matrix for the probe in the interaction picture. Its corresponding Schrodinger-picture quantity is

$$P_{1234}^{\text{S,probe}} = \sum_{\pm} A_{13}^{\text{probe},\pm} A_{24}^{\text{probe},\pm,*}, \quad (27)$$

$$A_{13}^{\text{probe},\pm} = \sqrt{\frac{2\pi}{\hbar}} \frac{e}{m_e} (\mathbf{A}_0^{\text{probe}} \cdot \mathbf{p}) \delta^{G,1/2}(\epsilon_1 - \epsilon_3 \pm \omega_{\text{probe}}). \quad (28)$$

The dielectric change detected by the probe is then

$$\text{Im}\Delta\epsilon = \frac{2\pi}{(\omega_{\text{probe}})^3 |A_0^{\text{probe}}|^2} \text{Tr}(H_0 \Delta\rho^{\text{probe}}). \quad (29)$$

Note that $\Delta\rho^{\text{probe}}$ contains $|A_0^{\text{probe}}|^2$ so that $\text{Im}\Delta\epsilon$ is independent of A_0^{probe} . The above $\text{Im}\Delta\epsilon$ is a functional of the density matrix according to Eq. 26 and is an extension of the usual independent-particle $\text{Im}\epsilon$ depending

on just occupation numbers.⁴⁴ After computing $\text{Im}\Delta\epsilon$ above, the real part $\text{Re}\Delta\epsilon$ can be obtained from the Kramers-Kronig relation. With the complete dielectric function change computed above, we can calculate Kerr and Faraday rotations.^{45,46} These correspond to the rotations of the polarization plane of a linearly polarized light, reflected by (Kerr) and transmitted through (Faraday) the material, after a pump excitation with a circularly-polarized light. Time-Resolved Kerr/Faraday Rotation (TRKR/TRFR) has been widely used to study spin dynamics of materials^{28,31,47}. Specifically, the Kerr rotation angle θ_K is given by

$$\theta_K = \text{Im} \frac{\sqrt{\epsilon_+} - \sqrt{\epsilon_-}}{1 - \sqrt{\epsilon_+} \sqrt{\epsilon_-}}, \quad (30)$$

where \pm denotes the left and right circular polarization, respectively.

III. COMPUTATIONAL DETAILS

The ground-state electronic structure, phonon, and e-ph matrix element calculations of GaAs are first calculated using Density Functional Theory (DFT) with relatively coarse k and q meshes in the JDFTx plane-wave DFT code.⁴⁸ We use the experimental lattice constant of 5.65315 Å,⁴⁹ and select the SCAN exchange-correlation functional for an accurate description of the electron effective mass.⁵⁰ The phonon calculations employ a $4 \times 4 \times 4$ supercell. We use Optimized Norm-Conserving Vanderbilt (ONCV) pseudopotentials⁵¹ with self-consistent spin-orbit coupling throughout, which we find converged at a plane-wave kinetic energy cutoff of 34 Ry. With these computational parameters, we find the effective mass of conduction electrons to be $0.054m_e$, close to the experimental value of $0.067m_e$.⁵² The resulting phonon dispersion of GaAs is also in agreement with experiments (see cutoff convergence tests and other details in Supplemental Materials⁵³).

We then transform all quantities from plane wave basis to maximally localized Wannier function basis⁵⁴, and interpolate them⁵⁵⁻⁶⁰ to substantially finer k and q meshes. The Wannier interpolation approach fully accounts for polar terms in the e-ph matrix elements and phonon dispersion relations, using the approach developed by Verdi and Giustino⁶¹. The Born effective charges and dielectric constants are calculated from open-source code QuantumESPRESSO⁶².

The fine k and q meshes are $288 \times 288 \times 288$ for simulations at 300 K and are finer at lower temperature, e.g., $792 \times 792 \times 792$ for simulations at 30 K. This is necessary to sample enough electronic states around band edges and for spin lifetime convergence within 20%. The computation of e-i and e-e matrix elements and the real-time dynamics simulations are done with a new custom code interfaced to JDFTx. The energy-conservation smearing parameter σ is chosen to be comparable or smaller than $k_B T$ for each calculation. Detailed convergence tests

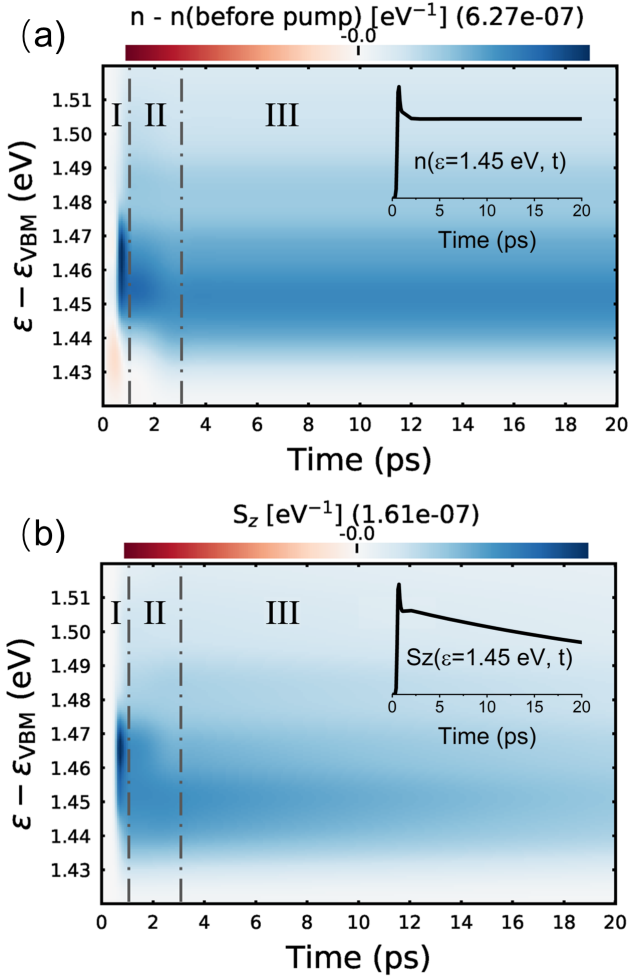


FIG. 1: The energy-resolved dynamics of carriers (a) $n(\epsilon, t)$ and (b) spins $S_z(\epsilon, t)$ of conduction electrons with a pump pulse centered at 0.5 ps. The insets on the top right of both panels show $n(\epsilon, t)$ and $S_z(\epsilon, t)$ at $\epsilon=1.45$ eV. The pump energy $\omega_{\text{pump}}=1.47$ eV higher than band gap 1.43 eV⁵². The width of the pump pulse τ_{pump} is 100 fs. The pump power is low at $0.01 \mu\text{J cm}^{-2}$. The dynamics can be approximately divided into three regions - Region I, II and III labeled in this figure. In Region I, the system is excited by a pump pulse. In Region II, pump processes are already finished, then both carriers and spins relax simultaneously. In Region III, carrier distribution stays unchanged while spins keep decaying.

of number of k points and energy range for electronic states at various smearings can be found in Supplemental Materials⁵³.

IV. RESULTS AND DISCUSSIONS

A. Time-resolved Kerr rotation and its relation to spin dynamics

In a TRKR experiment, a circularly-polarized pump pulse is used to excite valence electrons of the sample to

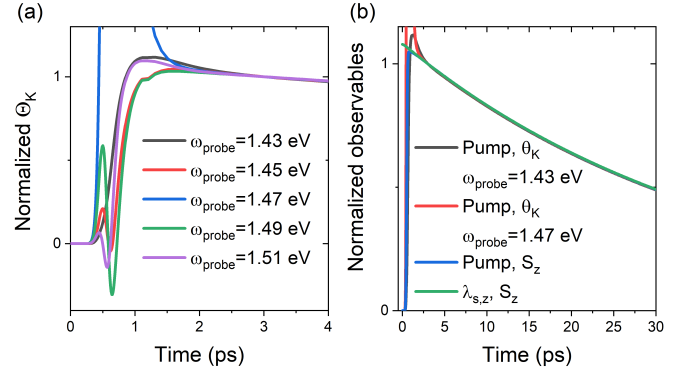


FIG. 2: (a) Compare the dynamics of Kerr rotation angle θ_K at different probe energies ω_{probe} excited by a pump pulse. (b) Compare relaxation of different observables - θ_K with different ω_{probe} (denoted by black and red lines) and S_z with initial spin imbalance generated by a pump pulse (Pump) or a test magnetic field along z direction $\lambda_{s,z} \sim 0.001 - 0.1$ Tesla (blue and green lines). $\omega_{\text{pump}}=1.47$ eV. The pump pulse is centered at 0.5 ps.

conduction bands. The transitions approximately satisfy the selection rule - $\Delta m_j = \pm 1$ for left and right circularly-polarized pulses, respectively, where m_j is secondary total angular momentum. TRKR works by measuring the changes of polarization of reflected light, which qualitatively is proportional to the small population imbalance of different electronic states with different m_j . Generally speaking, time evolution of Kerr rotation angle θ_K (see Eq. 30) is not equivalent to that of spin along the direction of reflected light, and in fact, they can be very different in some cases⁶³. There are few first-principles studies of TRKR considering both pump and scattering processes⁴⁴, and the relation between dynamics of θ_K and spin observable for general systems including GaAs has not yet been well examined.

Using our density-matrix approach, we are able to directly simulate the nonequilibrium ultrafast dynamics of optically excited systems during which the dynamics of different electronic quantities such as spin and carriers can be strongly coupled. Having temporal density matrix, we can further analyze the dynamics of various observables, including occupation, spin and Kerr rotation angle easily.

Figure 1 shows the energy-resolved dynamics of carriers $n(\epsilon, t)$ and spins $S_z(\epsilon, t)$. The energy-resolved observable $O(\epsilon)$ is defined as $\text{Re}[\sum_n o_{k,mn} \rho_{k,nm} \delta(\epsilon - \epsilon_{km})]$, where o is operator matrix. We can see that during the first ps (region I in Figure 1), both observables vary quickly due to the existence of the pump processes and both have their maximum at an energy slightly lower than the pump energy, 1.47 eV (slightly larger than the band gap 1.43 eV⁵² set by applying a scissor operator to DFT value), at a time shortly after the time center of the pump pulse - 0.5 ps. Interestingly, after pump being not active or after 0.8-1 ps, carriers and spins simultaneously relax until 2-3 ps (region II in Fig. 1a and 1b).

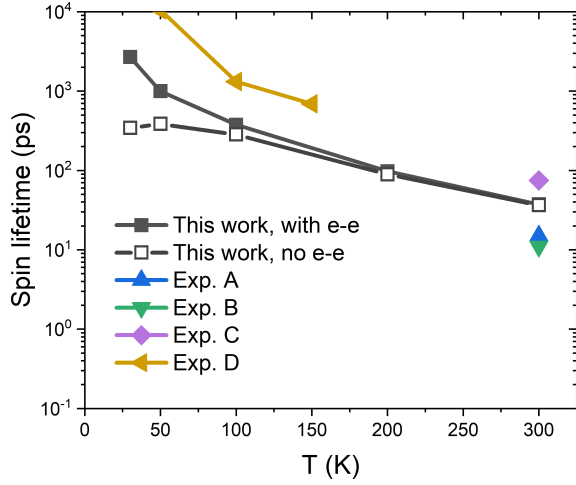


FIG. 3: Theoretical spin lifetime with (black solid square) and without (black empty square) the electron-electron scattering compared with experimental data. Exp. A, B, C and D are experimental data from Refs. 31,32,64 and 28, respectively.

Afterward (region III in Fig. 1a and 1b), carriers stay unchanged but spins $S_z(\epsilon, t)$ decay exponentially as shown in the insets of Fig. 1a and 1b.

We have further analyzed the dynamics of Kerr rotation angle θ_K and compared it with spin dynamics. From Fig. 2a, we can see that during pump processes and shortly after them (from 0 to 2 ps), $\theta_K(t)$ has strong oscillations and sensitive to the probe energy ω_{probe} . The ω_{probe} -sensitivity may be partly attributed to the energy dependence of carrier and spin dynamics. From Fig. 2a and 2b, it can be seen that after 3 ps (or in time region III defined in Fig. 1), θ_K with different ω_{probe} decay exactly the same. We can also find that with a pump pulse, relaxation time of the Kerr rotation is the same as that of S_z , i.e. $\tau_{s,z}$. Moreover, it turns out that $\tau_{s,z}$ does not depend on how spin imbalance is generated - by a pump pulse or by turning off a test magnetic field along z direction (see Sec. II A). This may indicate that if the system is not extremely far from equilibrium, spin relaxation along direction i is not sensitive to the way of generating spin imbalance, as long as the degrees of freedom other than S_i are not relevant or disappear in a short time. According to these observations, hereinafter, we will do real-time dynamics starting from a $\delta\rho$ generated by turning off a test magnetic field and fit $\tau_{s,z}$ from time evolution of S_z .

We have also studied the effects of ω_{pump} and pump power on spin relaxation of n -GaAs at 300 K. We find that ω_{pump} has very weak effects on spin relaxation but $\tau_{s,z}$ decreases with pump power. See more details in Appendix D.

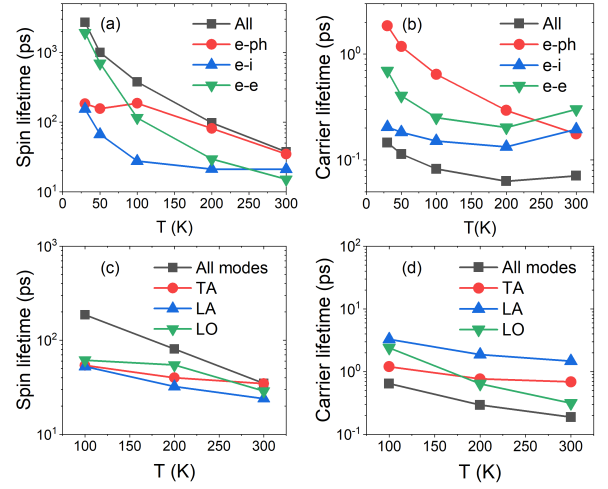


FIG. 4: Spin and carrier lifetimes of n -GaAs with $n_i = 2 \times 10^{16} \text{ cm}^{-3}$ with different scattering mechanisms and different phonon modes. In (a) and (b), “All” represents all the e-ph, e-i and e-e scattering mechanisms being considered. TA, LA and LO represent transverse acoustic, longitudinal acoustic and longitudinal optical modes, respectively. The carrier lifetimes $\bar{\tau}_p$ present are the inverse of averaged carrier scattering rates $\langle \tau_p^{-1} \rangle$. The method of carrier lifetime calculations is given in Appendix C. $\langle \rangle$ means taking average around chemical potential μ . For a state-resolved quantity A_{kn} , its average is defined as $\langle A \rangle = \sum_{kn} A_{kn} f'(\epsilon_{kn}) / \sum_{kn} f'(\epsilon_{kn})$, where f' is the derivative of Fermi-Dirac function.

B. Temperature-dependence of spin lifetime of GaAs

We then study $\tau_{s,z}$ of n -GaAs as a function of temperature at a moderate doping level ($2 \times 10^{16} \text{ cm}^{-3}$). For simplicity, we assume all impurities are fully ionized, so that the impurity density n_i is equal to the free carrier density n_{free} . We first compared our calculated spin lifetime with experimental results in Fig. 3. Our results of $\tau_{s,z}$ of n -GaAs give good agreement with experiments at various temperatures^{28,31,32,64}. Note that e-e scattering plays an essential role at low temperatures, i.e. by comparing with (black solid square) and without (black empty square) in Fig. 3. The correct temperature dependence of $\tau_{s,z}$ can be reproduced only if e-e scattering is included.

We further examine the contributions of different scattering mechanisms to carrier and spin lifetime respectively, as a function of temperature. Different from spin lifetime obtained from real-time DM dynamics including all scattering processes simultaneously, the carrier lifetime ($\bar{\tau}_p$) is defined through the inverse of the averaged carrier scattering rate (τ_p^{-1}): $\bar{\tau}_p = 1 / \langle \tau_p^{-1} \rangle$. Various scattering processes (e-e, e-i and e-ph) contribute to the total carrier scattering rates through $\tau_p^{-1} = \tau_{p,e-e}^{-1} + \tau_{p,e-i}^{-1} + \tau_{p,e-ph}^{-1}$. $\langle \rangle$ means taking average around chemical potential μ . For a state-resolved quantity A_{kn} , its average is defined as $\langle A \rangle = \sum_{kn} A_{kn} f'(\epsilon_{kn}) / \sum_{kn} f'(\epsilon_{kn})$,

where f' is the derivative of Fermi-Dirac function. For both carrier and spin lifetime, the most dominant scattering channel is the closest to the lifetime including all processes (black squares in both Fig. 4a and b). For spin relaxation in Fig. 4a, at low temperature below 50K, e-e scattering is the most dominant process as discussed above. However, the e-ph process becomes more dominant above 100K. On the other hand, for carrier relaxation in Fig. 4b, the e-i process is dominant over a wide temperature range from low to right below room temperature.

At room temperature, for both spin and carrier lifetimes, the e-ph scattering is the most important process (closest to the total lifetime with all scattering processes). This is different from the conclusion of Ref. 37 that e-e scattering enhances $\tau_{s,z}$ of n -GaAs by about 100% with moderate doping concentrations at room temperature. This is most likely a limitation of the semiclassical method employed therein that could have strongly overestimated the effects of e-e scattering.

Similarly, we also find that different phonon modes can play different roles in carrier and spin relaxations as shown in Fig. 4 (c) and (d). For example, at room temperature, LO (longitudinal optical) mode is most important for carrier relaxation but seems less important than TA (transverse acoustic) modes for spin relaxation. The situation is the opposite at 100 K where TA/LA is most important for carrier/spin relaxation. Our finding that TA modes are slightly more important than LO mode in spin relaxation at room temperature is different from what have been believed in previous model studies^{34,37}, where they declared that the electron-LO-phonon scattering dominates spin relaxation at high temperatures especially at room temperature. This disparity is most likely due to differences in the e-ph matrix elements and electronic quantities, where we used fully first-principles approaches instead of parameterized models in previous work.

In addition, we find the total spin lifetime is the longest when considering all scattering processes in Fig. 4a; in contrast, the carrier lifetime is the shortest including all scattering mechanism in Fig. 4b. This follows the inverse relation between spin and carrier lifetime in the phenomenological D'yakonov-Perel' (DP) mechanism for systems without inversion symmetry.^{2,14}

C. Doping-level-dependence of spin lifetime of GaAs

Fig. 5 shows the carrier and spin lifetimes with different doping density n_i at 30 K with individual and total scattering pathways, respectively. Similar to temperature dependence and phonon contributions, it is also found that the roles of different scattering mechanism vary considerably between spin and carrier relaxation processes. Specifically, for the carrier relaxation in Fig. 5b, except when n_i is very low (e.g. at 10^{14} cm^{-3}), the electron-

impurity scattering (e-i) dominates, similar to the case of spin lifetime over a large range of temperature at a moderate doping in Fig. 4b. On the other hand, for the spin relaxation in Fig. 5a, the e-e scattering dominates except at very high concentration (above 10^{17} cm^{-3}), while e-i scattering is only important in the very high doping region (close to or above 10^{17} cm^{-3}).

Fig. 5 shows the calculated τ_s has a maximum at $n_i = 1 - 2 \times 10^{16} \text{ cm}^{-3}$, and τ_s decreases fast with n_i going away from its peak position. This is in good agreement with the experimental finding in Ref. 28, which also reported τ_s at $n_i = 10^{16} \text{ cm}^{-3}$ is longer than τ_s at other lower and higher n_i at a low temperature (a few Kelvin). The n_i dependence of τ_s may be qualitatively interpreted from the commonly used empirical DP relation² for inversion-asymmetric systems, $\tau_{s,i} \sim \tau_{s,i}^{DP} = 1/[\bar{\tau}_p \cdot (\langle \Omega^2 \rangle - \langle \Omega_i^2 \rangle)]$, where Ω is the Larmor frequency corresponding to the "internal" magnetic field, which describes the SOC term induced by inversion asymmetry. For spin 1/2 systems, the internal magnetic field at \mathbf{k} ($\Omega_{\mathbf{k}}$) will induce an energy splitting $\Delta_{\mathbf{k}}$ and polarize the spin along the direction of $\Omega_{\mathbf{k}}$. Previously, $\Omega_{\mathbf{k}}$ was mostly obtained with model Hamiltonian with Dresselhaus SOC field⁶⁵, which is rather qualitative. Instead, we obtained \mathbf{k} -dependent internal magnetic field $\Omega_{\mathbf{k}}$ from first-principles calculations, by using $\Omega_{\mathbf{k},i} = \Delta_{\mathbf{k}} s_{\mathbf{k},i}^{exp}$, where $s_{\mathbf{k},i}^{exp}$ is the spin expectation value.

From Fig. 5, we find that with n_i from 10^{14} cm^{-3} to $5 \times 10^{15} \text{ cm}^{-3}$, carrier lifetime $\bar{\tau}_p$ decreases rapidly (black curve in Fig. 5b) and $\langle \Omega^2 \rangle - \langle \Omega_i^2 \rangle$ remains flat in Fig. 5c, which may explain why spin lifetime (τ_s) increases in Fig. 5a based on the DP relation; however, when $n_i > 10^{16} \text{ cm}^{-3}$, $\bar{\tau}_p$ decreases with a similar speed but $\langle \Omega^2 \rangle - \langle \Omega_i^2 \rangle$ experiences a sharp increase, which may explain why spin lifetime decreases in Fig. 5b and owns a maximum at 10^{16} cm^{-3} .

Note that although the above empirical DP relation is intuitive to understand the cause of doping-level-dependence of spin lifetime, it may break down when we evaluate individual scattering processes. For example, when n_i increases from 10^{14} cm^{-3} to 10^{15} cm^{-3} , both carrier lifetime $\bar{\tau}_p$ and spin lifetime $\tau_{s,z}$ due to e-i scattering decrease while the internal magnetic field remains unchanged. Moreover, the simple empirical relation cannot possibly explain the results from our first-principles calculations that the e-e and e-i scatterings have largely different contributions in carrier and spin relaxation. First-principles calculations are critical to provide unbiased mechanistic insights to spin and carrier relaxation of general systems.

V. CONCLUSIONS

In this article, we present a first-principles real-time density-matrix approach to simulate ultrafast spin-orbit-mediated spin dynamics in solids with arbitrary crystal symmetry. The complete *ab initio* descriptions of pump,

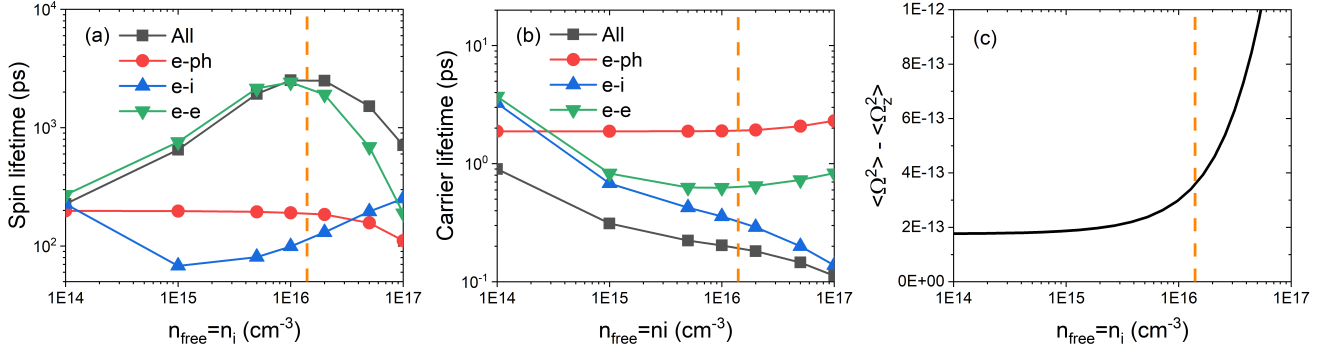


FIG. 5: (a) Spin and (b) carrier lifetimes of n -GaAs with different doping concentrations at 30 K with different scattering mechanisms. “All” represents all the e-ph, e-i and e-e scattering mechanisms being considered. (c) $\langle \Omega^2 \rangle - \langle \Omega_i^2 \rangle$ as a function of carrier density, where Ω is the Larmor frequency corresponding to the “internal” magnetic field computed from first-principles, which describes the SOC term induced by inversion asymmetry.

probe and three scattering processes - the electron-phonon, electron-impurity and electron-electron scattering in the density-matrix master equation, allows us to directly simulate the nonequilibrium ultrafast pump-probe measurements and makes our method applicable to any temperatures and doping levels. This method has been applied to simulate spin relaxation of n -GaAs. We confirm that relaxation time of Kerr rotation and that of spin observables are almost identical and find that relaxation time of spin polarization is relatively robust, i.e. insensitive to how spin imbalance is initialized. Furthermore, we have studied the temperature and doping-level dependences of spin lifetime and examined the roles of various scattering mechanisms. Overall our theoretical results are in excellent agreement with experiments. Importantly, our first-principles simulations provide rich and unbiased mechanistic insights of spin relaxation of n -GaAs: we pointed out that although at low temperatures and moderate doping concentrations e-i scattering dominates carrier relaxation, e-e scattering is the most dominant process in spin relaxation. The relative contributions of phonon modes also vary considerably between spin and carrier relaxation. Our method opens up the pathway to predict spin relaxation and decoherence for general materials and provide unbiased insights and guidelines to experimental materials design, which have the potential to revolutionize the field of spintronics and quantum information technologies.

Acknowledgements

We thank Hiroyuki Takenaka for helpful discussions. This work is supported by National Science Foundation under grant No. DMR-1956015. A. H. acknowledges support from the American Association of University Women(AAUW) fellowship program. This research used resources of the Center for Functional Nanomaterials, which is a US DOE Office of Science Facility, and the Scientific Data and Computing center, a component of

the Computational Science Initiative, at Brookhaven National Laboratory under Contract No. DE-SC0012704, the lux supercomputer at UC Santa Cruz, funded by NSF MRI grant AST 1828315, the National Energy Research Scientific Computing Center (NERSC) a U.S. Department of Energy Office of Science User Facility operated under Contract No. DE-AC02-05CH11231, the Extreme Science and Engineering Discovery Environment (XSEDE) which is supported by National Science Foundation Grant No. ACI-1548562⁶⁶, and resources at the Center for Computational Innovations at Rensselaer Polytechnic Institute.

Appendix A: Interaction Hamiltonian terms and matrix elements

Three interaction Hamiltonian terms in Eq. 3 read

$$H_{e-ph} = \sum_{12q\lambda} c_1^\dagger c_2 \left(g_{12}^{q\lambda-} b_{q\lambda} + g_{12}^{q\lambda+} b_{q\lambda}^\dagger \right), \quad (31)$$

$$H_{e-i} = n_i V_{\text{cell}} \sum_{12} c_1^\dagger c_2 g_{12}^i, \quad (32)$$

$$H_{e-e} = \sum_{1234} c_1^\dagger c_2^\dagger c_3 c_4 g_{1234}^{e-e}. \quad (33)$$

The e-ph matrix $g^{q\lambda\pm}$ are computed with self-consistent spin-orbit coupling and Wannier interpolation by the supercell method. We focus on the e-i matrix g^i and e-e one g^{e-e} , which are the following

$$g_{12}^i = \langle 1 | V^i | 3 \rangle, \quad (34)$$

$$g_{1234}^{e-e} = \langle 1(r) | \langle 2(r') | V(r-r') | 3(r) \rangle | 4(r') \rangle, \quad (35)$$

where V^i is the impurity potential and $V(r-r')$ is the screened electron-electron interaction. We assume all impurities are ionized, for which we may safely express V^i as the product of the impurity charge Z and the screened

Coulomb potential^{41,67}. Therefore, the computation of the screened Coulomb potential is of key importance in the calculations of g^i and g^{e-e} .

Currently, we use the static RPA (Random Phase Approximation) dielectric function for the screening and neglect local-field effects. We then show the e-e self-energy ($\text{Im}\Sigma$) obtained with such dielectric function well reproduces the one obtained with dynamically screened Coulomb interaction with full RPA dielectric matrix in the relevant energy range in Fig. 6. The dielectric function has the form

$$\epsilon(\mathbf{q}) = \epsilon_s \epsilon^{\text{intra}}(\mathbf{q}), \quad (36)$$

where ϵ_s is the static background dielectric constant and can be calculated by Density Functional Perturbation Theory (DFPT)⁶⁸. $\epsilon^{\text{intra}}(\mathbf{q})$ is the intraband contribution which involves only states with free carriers and is critical for doped semiconductors. It is computed using Random Phase Approximation (RPA),

$$\epsilon^{\text{intra}}(\mathbf{q}) = 1 - V^{\text{bare}}(\mathbf{q}) \sum_{\mathbf{k}mn} \left(\frac{f_{\mathbf{k}-\mathbf{q},m} - f_{\mathbf{k}n}}{\epsilon_{\mathbf{k}-\mathbf{q},m} - \epsilon_{\mathbf{k},n}} \times \frac{\langle u_{\mathbf{k}-\mathbf{q},m} | u_{\mathbf{k}n} \rangle}{|\langle u_{\mathbf{k}-\mathbf{q},m} | u_{\mathbf{k}n} \rangle|^2} \right), \quad (37)$$

where the sum runs over only states having free carriers, e.g., for a n-doped semiconductor, m and n are conduction band indices. $V^{\text{bare}}(\mathbf{q}) = e^2 / (V_{\text{cell}} \epsilon_0 q^2)$ is the bare Coulomb potential with V_{cell} the unit cell volume and ϵ_0 vacuum permittivity. $u_{\mathbf{k}n}$ is the periodic part of the Bloch wave function.

We then have the matrix elements in reciprocal space,

$$g_{13}^i = Z V^{\text{scr}}(\mathbf{q}_{13}) \langle u_1 | u_3 \rangle, \quad (38)$$

$$g_{1234}^{e-e} = V^{\text{scr}}(\mathbf{q}_{13}) \delta_{\mathbf{k}_1+\mathbf{k}_2, \mathbf{k}_3+\mathbf{k}_4} \langle u_1 | u_3 \rangle \langle u_2 | u_4 \rangle, \quad (39)$$

$$V^{\text{scr}}(\mathbf{q}_{13}) = V^{\text{bare}}(\mathbf{q}_{13}) / \epsilon(\mathbf{q}_{13}), \quad (40)$$

where $V^{\text{scr}}(\mathbf{q})$ is the screened Coulomb potential and $\mathbf{q}_{13} = \mathbf{k}_1 - \mathbf{k}_3$. $\delta_{\mathbf{k}_1+\mathbf{k}_2, \mathbf{k}_3+\mathbf{k}_4}$ is Kronecker delta function and means $\mathbf{k}_1 + \mathbf{k}_2 = \mathbf{k}_3 + \mathbf{k}_4$. $\langle u_1 | u_3 \rangle$ is the overlap matrix element between two periodic parts of the Bloch wave functions.

Appendix B: The treatment of holes for n-GaAs

For n-GaAs, it is unnecessary to treat scattering processes of holes exactly. This is because: (i) When ρ is initialized by turning off a test magnetic field, the dynamics of holes will be irrelevant as hole concentration is negligible; (ii) When ρ is initialized by a pump pulse, there are some holes being excited. But since the time scale of hole spin relaxation, ~ 110 fs at 300 K²⁹, is much faster

than the time scale of the Kerr rotation, the hole scattering processes should have little effects on global Kerr-rotation or spin dynamics. Therefore, when the pump process is active, the dynamics of holes are described approximately by assuming the time derivative of the hole density matrix satisfies $d\rho/dt = -(\rho - \rho^{\text{eq}})/\tau_{\text{hole}}$ with $\tau_{\text{hole}} = 110$ fs at 300 K. And we have confirmed the real-time dynamics is insensitive to the choice of τ_{hole} .

Appendix C: Carrier scattering rate and $\text{Im}\Sigma$ from the density-matrix approach

At the semiclassical limit, density matrix ρ is replaced by occupation f then the scattering term reads:

$$\frac{df_1}{dt}|_c = \sum_{2 \neq 1} [(1 - f_1) P_{11,22}^c f_2 - (1 - f_2) P_{22,11}^c f_1], \quad (41)$$

using the facts that $P_{11,22}$ is real and “2=1” term is zero. “c” represent a scattering channel. Note that the weights of \mathbf{k} points must be considered when doing sum over \mathbf{k} points.

Suppose f_1 is perturbed from its equilibrium value by δf_1 , i.e., $f_1 = f_1^{\text{eq}} + \delta f_1$, then insert f_1 after perturbation into the Eq. 41 and linearize it,

$$\frac{df_1}{dt}|_c = - \sum_{2 \neq 1} [P_{11,22}^c f_2 + (1 - f_2) P_{22,11}^c] \delta f_1, \quad (42)$$

using the fact that $\delta P_{11,22}$ is always zero, even for the e-e scattering.

Define carrier relaxation time of state “1” $\tau_{p,1}^c$ by $\frac{df_1}{dt}|_c = -\frac{\delta f_1}{\tau_{p,1}^c}$, we have

$$\frac{1}{\tau_{p,1}^c} = \sum_{2 \neq 1} [P_{11,22}^c f_2 + (1 - f_2) P_{22,11}^c]. \quad (43)$$

The linewidth or the imaginary part of the self-energy for the scattering channel c is related to the carrier relaxation time by $\text{Im}\Sigma_1^c = \hbar / (2\tau_{p,1}^c)$.

Using Eq. 43, we have calculated the e-ph scattering rates and they are in good agreement with previous theoretical results⁶⁹. For e-ph scattering, Eq. 43 will reproduce the imaginary part of the well-known Fan-Migdal self-energy^{70,71}.

For e-i scatterings, we have

$$\frac{1}{\tau_{p,1}^{e-i}} = \frac{2\pi}{\hbar} n_i V_{\text{cell}} \sum_2 |g_{12}^i|^2 \delta^G(\epsilon_1 - \epsilon_2). \quad (44)$$

The above equation is consistent with Refs. 41 and 67.

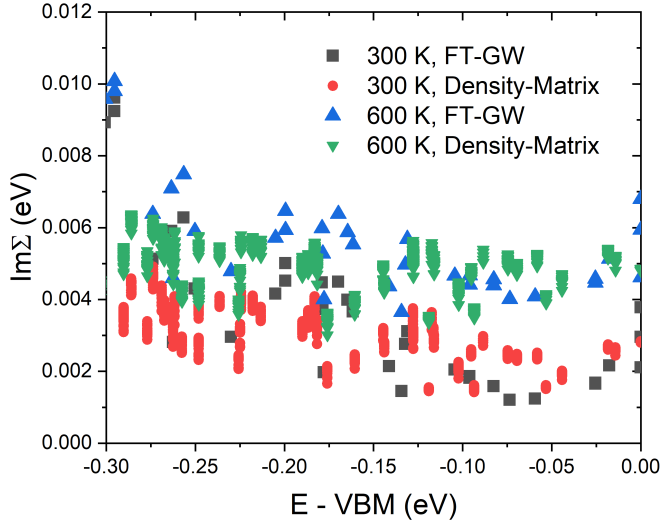


FIG. 6: $\text{Im}\Sigma$ due to e-e scattering of valence electrons of p-type silicon by Eq. 45 based on the density-matrix approach (Density-Matrix) compared with those calculated by the finite-temperature GW method (FT-GW)^{72,73}. μ is set to 0.05 eV lower than Valence Band Maximum (VBM). For simplicity, SOC is not considered in this test.

For e-e scattering, neglecting the exchange contribution, we have

$$\frac{1}{\tau_1} = \frac{2\pi}{\hbar} \sum_{2 \neq 1, 34} |A_{1324}|^2 [f_2 f_4 (1 - f_3) + (1 - f_2) f_3 (1 - f_4)]. \quad (45)$$

To verify our implementation of e-e scattering term, we have calculated $\text{Im}\Sigma$ due to e-e scattering of valence electrons of p-type silicon based on the above equation and compare it with those calculated by the finite-temperature GW method,^{72,73} as implemented for first-principles calculations in JDFTx.⁴⁸ The JDFTx implementation, in turn, has been benchmarked to reproduce the expected dependence with temperature and carrier energy, $\text{Im}\Sigma_{ee} \propto (\varepsilon - \varepsilon_F)^2 + (\pi k_B T)^2$, as expected for metals.⁶⁰ From Fig. 6, we can see the results by two methods agree well for the energy range close to the Fermi level which is relevant to e-e scatterings due to energy conservation. This verifies of our implementation of e-e scattering part.

Appendix D: The effects of ω_{pump} and pump power on spin relaxation of GaAs at 300 K

From Fig. 7, we can easily see that variation of ω_{pump} has very weak effects on spin dynamics of *n*-GaAs at 300 K.

In Fig. 8, we study the effects of the pump power I_{pump} on spin relaxation. Firstly, we can see that in the low pump power region or when $I_{\text{pump}} < 1 \mu\text{J}/\text{cm}^2$, the excitation density increases linearly with I_{pump} but when

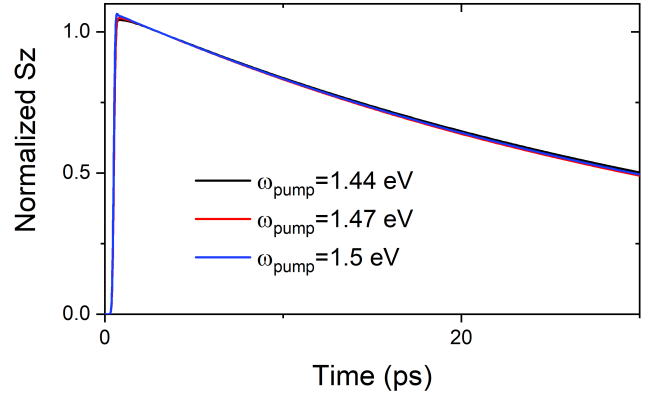


FIG. 7: $S_z(t)$ of *n*-GaAs with $n_i = 2 \times 10^{16} \text{ cm}^{-3}$ at 300 K with different pump pulse energies (ω_{pump}).

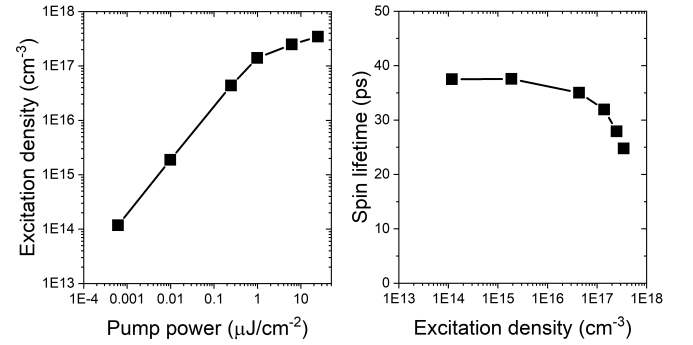


FIG. 8: The excitation density as a function of the pump power (left panel) and the spin lifetime as a function of the excitation density generated by a pump pulse (right panel) for *n*-GaAs with $n_i = 10^{14} \text{ cm}^{-3}$ at 300 K. $\omega_{\text{pump}} = 1.47 \text{ eV}$.

$I_{\text{pump}} > 1 \mu\text{J}/\text{cm}^2$, the excitation density will increase slower. This is because in high power cases, during the excitation by a pump pulse, a significant amount of conduction states have been already filled, which will reduce the probability of the transitions from valence bands to conduction bands. From the right panel of Fig. 8, we find that at 300 K, spin lifetime of *n*-GaAs decreases with the excitation density and the pump power. This dependence may be explained based on the empirical relation² $\tau_{s,i} \sim \tau_{s,i}^{DP} = 1/[\bar{\tau}_p \cdot (\langle \Omega^2 \rangle - \langle \Omega_i^2 \rangle)]$ as we discussed in Sec. IV B. At 300 K, generally $\langle \Omega^2 \rangle - \langle \Omega_i^2 \rangle$ will increase with increasing free carrier density (through an increase of excitation density here), similar to what we find at 30 K shown in Fig. 5(c). On the other hand, $\bar{\tau}_p$ due to the electron-phonon scattering, which dominates carrier relaxation at 300 K, is less sensitive to the variation of the excitation density. Therefore, it is the increase of $\langle \Omega^2 \rangle - \langle \Omega_i^2 \rangle$ causing the decrease of spin lifetime when increasing excitation density.

References

- ¹ D. D. Awschalom, R. Hanson, J. Wrachtrup, and B. B. Zhou, *Nat. Photon.* **12**, 516 (2018).
- ² I. Žutić, J. Fabian, and S. D. Sarma, *Rev. Mod. Phys.* **76**, 323 (2004).
- ³ F. Meier and B. P. Zakharchenya, *Optical orientation* (Elsevier, 2012).
- ⁴ D. Giovanni, H. Ma, J. Chua, M. Grätzel, R. Ramesh, S. Mhaisalkar, N. Mathews, and T. C. Sum, *Nano Lett.* **15**, 1553 (2015).
- ⁵ M. Johnson and R. H. Silsbee, *Phys. Rev. Lett.* **55**, 1790 (1985).
- ⁶ A. Aysar, H. Ochoa, F. Guinea, B. Özyilmaz, B. van Wees, and I. J. Vera-Marun, *Rev. Mod. Phys.* **92**, 021003 (2020).
- ⁷ F. Wu, A. Galatas, R. Sundararaman, D. Rocca, and Y. Ping, *Phys. Rev. Mater.* **1**, 071001 (2017).
- ⁸ T. J. Smart, F. Wu, M. Govoni, and Y. Ping, *Phys. Rev. Materials* **2**, 124002 (2018).
- ⁹ F. Wu, T. J. Smart, J. Xu, and Y. Ping, *Phys. Rev. B* **100**, 081407 (2019).
- ¹⁰ F. Wu, D. Rocca, and Y. Ping, *J. Mater. Chem. C* **7**, 12891 (2019).
- ¹¹ T. J. Smart, K. Li, J. Xu, and Y. Ping, (2020), arXiv:2009.02830 .
- ¹² R. Elliott, *Phys. Rev.* **96**, 266 (1954).
- ¹³ Y. Yafet, in *Solid State Phys.*, Vol. 14 (Elsevier, 1963) pp. 1–98.
- ¹⁴ M. Dyakonov and V. Perel, *Soviet Physics Solid State, USSR* **13**, 3023 (1972).
- ¹⁵ A. W. Cummings, J. H. Garcia, J. Fabian, and S. Roche, *Phys. Rev. Lett.* **119**, 206601 (2017).
- ¹⁶ M. Wu, J. Jiang, and M. Weng, *Phys. Rep.* **493**, 61 (2010).
- ¹⁷ O. D. Restrepo and W. Windl, *Phys. Rev. Lett.* **109**, 166604 (2012).
- ¹⁸ J. Park, J.-J. Zhou, and M. Bernardi, *Phys. Rev. B* **101**, 045202 (2020).
- ¹⁹ C. Illg, M. Haag, and M. Fähnle, *Phys. Rev. B* **88**, 214404 (2013).
- ²⁰ M. A. Marques, N. T. Maitra, F. M. Nogueira, E. K. Gross, and A. Rubio, *Fundamentals of time-dependent density functional theory*, Vol. 837 (Springer Science & Business Media, 2012).
- ²¹ K. Capelle, G. Vignale, and B. Györfy, *Phys. Rev. Lett.* **87**, 206403 (2001).
- ²² Z. Chen and L.-W. Wang, *Sci. Adv.* **5**, eaau8000 (2019).
- ²³ S. R. Acharya, V. Turkowski, G. Zhang, and T. S. Rahman, *Phys. Rev. Lett.* **125**, 017202 (2020).
- ²⁴ K. Krieger, J. Dewhurst, P. Elliott, S. Sharma, and E. Gross, *J. Chem. Theory Comput.* **11**, 4870 (2015).
- ²⁵ J. Xu, A. Habib, S. Kumar, F. Wu, R. Sundararaman, and Y. Ping, *Nat. Commun.* **11**, 1 (2020).
- ²⁶ D. Taj, R. Iotti, and F. Rossi, *Eur. Phys. J. B* **72**, 305 (2009).
- ²⁷ R. Rosati, R. C. Iotti, F. Dolcini, and F. Rossi, *Phys. Rev. B* **90**, 125140 (2014).
- ²⁸ J. Kikkawa and D. Awschalom, *Phys. Rev. Lett.* **80**, 4313 (1998).
- ²⁹ D. Hilton and C. Tang, *Phys. Rev. Lett.* **89**, 146601 (2002).
- ³⁰ Y. Ohno, R. Terauchi, T. Adachi, F. Matsukura, and H. Ohno, *Phys. Rev. Lett.* **83**, 4196 (1999).
- ³¹ A. Kimel, F. Bentivegna, V. Gridnev, V. Pavlov, R. Pisarev, and T. Rasing, *Phys. Rev. B* **63**, 235201 (2001).
- ³² P. Hohage, G. Bacher, D. Reuter, and A. Wieck, *Appl. Phys. Lett.* **89**, 231101 (2006).
- ³³ Z. Yu, S. Krishnamurthy, M. Van Schilfgaarde, and N. Newman, *Phys. Rev. B* **71**, 245312 (2005).
- ³⁴ J. Jiang and M. Wu, *Phys. Rev. B* **79**, 125206 (2009).
- ³⁵ M. Krauß, H. Schneider, R. Bratschitsch, Z. Chen, and S. Cundiff, *Phys. Rev. B* **81**, 035213 (2010).
- ³⁶ M. D. Mower, G. Vignale, and I. Tokatly, *Phys. Rev. B* **83**, 155205 (2011).
- ³⁷ G. Marchetti, M. Hodgson, J. McHugh, R. Chantrell, and I. D’Amico, *Materials* **7**, 2795 (2014).
- ³⁸ F. Rossi and T. Kuhn, *Rev. Mod. Phys.* **74**, 895 (2002).
- ³⁹ R. Rosati, *Microscopic modeling of energy dissipation and decoherence in nanoscale materials and devices*, Ph.D. thesis, Polytechnic University of Turin (2014).
- ⁴⁰ F. Giustino, *Rev. Mod. Phys.* **89**, 015003 (2017).
- ⁴¹ D. Chattopadhyay and H. Queisser, *Rev. Mod. Phys.* **53**, 745 (1981).
- ⁴² L. Hedin, *Phys. Rev.* **139**, A796 (1965).
- ⁴³ M. D’Alessandro and D. Sangalli, *Phys. Rev. B* **102**, 104437 (2020).
- ⁴⁴ A. Molina-Sánchez, D. Sangalli, L. Wirtz, and A. Marini, *Nano Lett.* **17**, 4549 (2017).
- ⁴⁵ T. Gasche, M. Brooks, and B. Johansson, *Phys. Rev. B* **53**, 296 (1996).
- ⁴⁶ N. Mainkar, D. A. Browne, and J. Callaway, *Phys. Rev. B* **53**, 3692 (1996).
- ⁴⁷ J. Gupta, D. Awschalom, A. L. Efros, and A. Rodina, *Phys. Rev. B* **66**, 125307 (2002).
- ⁴⁸ R. Sundararaman, K. Letchworth-Weaver, K. A. Schwarz, D. Gunceler, Y. Ozhables, and T. Arias, *SoftwareX* **6**, 278 (2017).
- ⁴⁹ O. Madelung, U. Rössler, and M. Schulz, *Group IV Elements, IV-IV and III-V Compounds. Part a - Lattice Properties* (Springer-Verlag Berlin Heidelberg, 2001).
- ⁵⁰ J. Sun, A. Ruzsinszky, and J. P. Perdew, *Phys. Rev. Lett.* **115**, 036402 (2015).
- ⁵¹ D. Hamann, *Phys. Rev. B* **88**, 085117 (2013).
- ⁵² O. Madelung, *Semiconductors* (Springer, 1987).
- ⁵³ “See supplemental material at [url] for convergence tests, band structure and phonon dispersions.” .
- ⁵⁴ N. Marzari and D. Vanderbilt, *Phys. Rev. B* **56**, 12847 (1997).
- ⁵⁵ A. M. Brown, R. Sundararaman, P. Narang, W. A. Goddard, and H. A. Atwater, *ACS Nano* **10**, 957 (2016).
- ⁵⁶ F. Giustino, M. L. Cohen, and S. G. Louie, *Phys. Rev. B* **76**, 165108 (2007).
- ⁵⁷ P. Narang, L. Zhao, S. Claybrook, and R. Sundararaman, *Adv. Opt. Mater.* **5**, 1600914 (2017).
- ⁵⁸ A. M. Brown, R. Sundararaman, P. Narang, A. M. Schwartzberg, W. A. Goddard III, and H. A. Atwater, *Phys. Rev. Lett.* **118**, 087401 (2017).
- ⁵⁹ A. Habib, R. Florio, and R. Sundararaman, *J. Opt.* **20**, 064001 (2018).
- ⁶⁰ A. M. Brown, R. Sundararaman, P. Narang, W. A. Goddard III, and H. A. Atwater, *Phys. Rev. B* **94**, 075120 (2016).
- ⁶¹ C. Verdi and F. Giustino, *Phys. Rev. Lett.* **115**, 176401 (2015).
- ⁶² P. Giannozzi, S. Baroni, N. Bonini, M. Calandra, R. Car, C. Cavazzoni, D. Ceresoli, G. L. Chiarotti, M. Cococ-

- cioni, I. Dabo, *et al.*, J. Condens. Matter Phys. **21**, 395502 (2009).
- ⁶³ L. Yang, N. A. Sinitsyn, W. Chen, J. Yuan, J. Zhang, J. Lou, and S. A. Crooker, Nat. Phys. **11**, 830 (2015).
- ⁶⁴ A. Bungay, S. Popov, I. Shatwell, and N. Zheludev, Phys. Lett. A **234**, 379 (1997).
- ⁶⁵ G. Dresselhaus, Phys. Rev. **100**, 580 (1955).
- ⁶⁶ J. Towns, T. Cockerill, M. Dahan, I. Foster, K. Gaither, A. Grimshaw, V. Hazlewood, S. Lathrop, D. Lifka, G. D. Peterson, R. Roskies, J. R. Scott, and N. Wilkins-Diehr, Comput. Sci. Eng. **16**, 62 (2014).
- ⁶⁷ C. Jacoboni, *Theory of electron transport in semiconductors: a pathway from elementary physics to nonequilibrium Green functions*, Vol. 165 (Springer Science & Business Media, 2010).
- ⁶⁸ X. Wu, D. Vanderbilt, and D. Hamann, Phys. Rev. B **72**, 035105 (2005).
- ⁶⁹ J.-J. Zhou and M. Bernardi, Physical Review B **94**, 201201 (2016).
- ⁷⁰ H. Fan, Phys. Rev. **82**, 900 (1951).
- ⁷¹ A. Migdal, Sov. Phys. JETP **7**, 996 (1958).
- ⁷² L. X. Benedict, C. D. Spataru, and S. G. Louie, Phys. Rev. B **66**, 085116 (2002).
- ⁷³ J. Kas and J. Rehr, Phys. Rev. Lett. **119**, 176403 (2017).